

# Observational Signatures of Exact Black Hole Solutions in a Dark Matter Halo

Azalbek Boltaev,<sup>1,\*</sup> Tursunali Xamidov,<sup>2,3,4,†</sup> and Sanjar Shaymatov<sup>2,5,4,‡</sup>

<sup>1</sup>*New Uzbekistan University, Movarounnahr str. 1, Tashkent 100000, Uzbekistan*

<sup>2</sup>*Institute of Fundamental and Applied Research,  
National Research University TIAME, Kori Nijoziy 39, Tashkent 100000, Uzbekistan*

<sup>3</sup>*Institute for Theoretical Physics and Cosmology,  
Zhejiang University of Technology, Hangzhou 310023, China*

<sup>4</sup>*Tashkent State Technical University, 100095 Tashkent, Uzbekistan*

<sup>5</sup>*Tashkent University of Applied Sciences, Gavhar Str. 1, Tashkent 100149, Uzbekistan*

(Dated: March 19, 2026)

In this work, we derive novel exact solutions describing Schwarzschild-like black holes (BHs) embedded in a Dehnen-type dark matter (DM) halo density profile and investigate their geometric, dynamical, and observational signatures arising from such geometries. We begin by analyzing the horizon structure and spacetime curvature invariants, as well as examining the energy conditions associated with the DM halo. Subsequently, we study the influence of the DM halo on both timelike and null geodesics in the resulting geometry. Finally, we obtain observational constraints on the DM halo parameters by comparing the model predictions with weak-field data from Mercury and the S2 star orbit, as well as strong-field observations from the Event Horizon Telescope (EHT), GRAVITY, and combined (EHT+GRAVITY) datasets for M87\* and Sgr A\*, employing Bayesian inference and Markov Chain Monte Carlo (MCMC) methods to determine the best-fit values and corresponding upper limits of the model parameters. Our analysis provides valuable insight into probing the potential influence of DM halo environments on spacetime geometry and observable properties of astrophysical BHs, offering an alternative perspective on BH–DM interactions.

PACS numbers:

## I. INTRODUCTION

Despite numerous experimental tests in both the weak- and strong-field regimes, General Relativity (GR) still faces significant challenges and unresolved issues. In particular, it does not provide a satisfactory description of black hole (BH) singularities, nor does it explain the unknown nature of dark matter (DM) and dark energy. Recent observations by the EHT [1, 2] and LIGO–Virgo [3, 4] have confirmed key predictions of BH physics. Nevertheless, GR is generally regarded as an incomplete theory. Consequently, BHs continue to be intensively investigated using these remarkable observational advances, and the origin and fundamental nature of DM remain among the major open problems in modern cosmology. In astrophysical scenarios, supermassive BHs located at galactic centers are expected to reside in complex environments. Observational and theoretical studies further suggest that they are embedded within DM halos [5, 6]. Moreover, compelling evidence for DM arises from galactic rotation curves [7], observations of galaxy clusters such as the Bullet Cluster [8], and the formation of large-scale cosmic structures [9].

Astrophysical observations indicate that dark matter (DM) accounts for about  $\sim 90\%$  of the mass of a galaxy, while the remaining  $\sim 10\%$  consists of luminous bary-

onic matter [10]. Many large spiral and elliptical galaxies are also observed to host central supermassive BHs embedded within these DM halos [1, 2, 11, 12]. Extensions of the Standard Model predict several viable DM candidates, such as weakly interacting massive particles (WIMPs), axions, and neutrinos [13–16]. In such scenarios, where interactions with Standard Model particles are extremely weak, the properties of DM are primarily probed through its gravitational effects. Hence, DM is expected to accumulate around supermassive BHs at galactic centers, where it may potentially affect the extreme [17] and intermediate [18, 19] mass ratio inspirals and provide insights into the DM halo profile. Such halos are also essential for explaining galactic rotation curves and cluster dynamics [6–8, 20].

BHs, which are believed to reside within DM environments, provide a natural laboratory for studying BH–DM interactions. Given the fundamental role of DM halos, investigating this interplay and developing viable DM models is essential for improving our understanding of the nature of DM. To this end, BH solutions embedded in DM halos have been modeled using several analytical profiles, including the Einasto, Navarro–Frenk–White, Burkert, and Dehnen profiles [21–30]. Alternative approaches involve DM distributions associated with phantom scalar fields and analytical supermassive BH solutions within DM halos [31–38].

It is important to emphasize that a DM halo surrounding a BH not only affects the particle dynamics but also modifies the spacetime geometry. This may alter the horizon structure and leave observable signatures in quantities such as the innermost stable circular orbit

\*Electronic address: [azalbekboltaev2@gmail.com](mailto:azalbekboltaev2@gmail.com)

†Electronic address: [xamidovtursunali@gmail.com](mailto:xamidovtursunali@gmail.com)

‡Electronic address: [sanjar@astrin.uz](mailto:sanjar@astrin.uz)

(ISCO) and BH shadows, etc. Such DM–BH interactions have also been explored in the context of the Dehnen-type halo framework. For example, BH solutions embedded in Dehnen-type DM halos have been proposed to model ultra-faint dwarf galaxies [28]. Subsequent studies have further explored BH solutions with different DM halo density profiles [27, 29, 30], investigating their effects on quasinormal modes, BH shadows, and gravitational waveforms, as well as constraining DM halo parameters [39–43].

Motivated by these findings, in this paper we present Schwarzschild-like BH solutions in a Dehnen-type DM halo with a density profile  $(1, 4, \gamma)$ . We analyze space-time curvature invariants, examine the associated energy conditions, and investigate the influence of the DM halo on timelike and null geodesics. Constraints on the DM halo parameters are obtained from weak-field tests using Mercury and S2 star observations, as well as from strong-field data including EHT, GRAVITY, and combined (EHT+GRAVITY) observations of M87\* and Sgr A\* by employing Bayesian inference and Markov Chain Monte Carlo (MCMC) methods to estimate the model parameters.

The paper is organized as follows: In Sec. II, we present novel exact solutions of the Einstein–Maxwell equations describing Schwarzschild-like BHs embedded in a DM halo characterized by a Dehnen-type density profile, and analyze their horizon structure. In Sec. III, we examine the spacetime curvature invariants and investigate the energy conditions associated with the DM halo. We then study the influence of the DM halo on both timelike and null geodesics in the resulting geometry for the density profile  $(1, 4, \gamma)$ . In Sec. IV, we constrain the characteristic DM halo parameters using weak-field observational data from Mercury and the orbit of the S2 star. In Sec. V, we extend the analysis to the strong-field regime by employing observations from the EHT and GRAVITY, as well as combined (EHT+GRAVITY) datasets for M87\* and Sgr A\*. Using Bayesian inference and MCMC methods, we obtain constraints on the characteristic density  $\rho_s$  and scale radius  $r_s$  of the DM halo. Finally, we summarize our results and conclusions in Sec. VI.

## II. SCHWARZSCHILD-LIKE BLACK HOLE SPACETIME WITH THE DARK MATTER HALO

Here, we begin by considering a spherically symmetric background spacetime with a DM halo distribution, modeling through a Dehnen-type density profile. With this in mind, we derive an exact solution of the Einstein–Maxwell equations describing a Schwarzschild-like BH embedded in a Dehnen-type DM halo mass distribution [44]. To this end, we first specify the form of the density profile that yields corresponding Dehnen-type DM halo mass distribution. In general, it can be written

as

$$\rho(r) = \rho_s \left(\frac{r}{r_s}\right)^{-\gamma} \left[ \left(\frac{r}{r_s}\right)^\alpha + 1 \right]^{\frac{\gamma-\beta}{\alpha}}, \quad (1)$$

with the characteristic density  $\rho_s$  and characteristic scale  $r_s$  of the DM halo. In addition to these characteristic DM halo parameters,  $\alpha$ ,  $\beta$  and  $\gamma$  determine specific shape of the density profile, referred to as the free parameters of the profile. For instance, the parameter  $\gamma$  is restricted to the interval  $0 \leq \gamma \leq 3$ . Taking this into account, in this work, we choose the following specific profile parameters  $(\alpha, \beta, \gamma) = (1, 4, \gamma)$ . Following Eq. (1), we then define the DM halo mass profile as

$$M_D(r) = \int_0^r 4\pi\rho(r_1)r_1^2 dr_1. \quad (2)$$

We then turn to write the line elements of a static and spherically symmetric spacetime surrounded by the DM halo, modeling through redshift  $A(r)$  and shape  $B(r)$  functions

$$ds^2 = -A(r)dt^2 + \frac{dr^2}{B(r)} + r^2 d\Omega^2, \quad (3)$$

with the solid angle with spherical coordinates  $d\Omega^2 = d\theta^2 + \sin^2\theta d\phi^2$ . For that the Einstein field equation reads as ([29, 45]):

$$R_{\mu\nu} - \frac{1}{2}g_{\mu\nu}R = 8\pi T_{\mu\nu}(D), \quad (4)$$

where  $T_{\mu\nu}(D)$  refers to the source part. It is then given by

$$T_{\mu}^{\nu}(D) = g^{\nu\alpha}T_{\mu\alpha}(D) = \text{diag}[-\rho(r), P_r(r), P_t(r), P_t(r)],$$

referred to as the energy-momentum tensor of the DM halo spacetime geometry. Given the energy-momentum tensor, we write the Einstein's field equations as follows:

$$B(r) \left( \frac{1}{r} \frac{B'(r)}{B(r)} + \frac{1}{r^2} \right) - \frac{1}{r^2} = 8\pi T_t^t(D), \quad (5)$$

$$B(r) \left( \frac{1}{r} \frac{A'(r)}{A(r)} + \frac{1}{r^2} \right) - \frac{1}{r^2} = 8\pi T_r^r(D), \quad (6)$$

$$\begin{aligned} \frac{B(r)}{2A(r)} \left( A''(r) - \frac{A'(r)^2}{2A(r)} + \frac{A'(r)}{r} \right) + \frac{B'(r)}{2} \left( \frac{A'(r)}{2A(r)} + \frac{1}{r} \right) \\ = 8\pi T_{\theta}^{\theta}(D) = 8\pi T_{\phi}^{\phi}(D) = 8\pi P_t(r). \end{aligned} \quad (7)$$

From the temporal component of Einstein's equations, Eq. (5), it is the first-order differential equation with respect to  $B'(r)$  and is rewritten as

$$\frac{d}{dr} \left[ r(B(r) - 1) \right] = -8\pi r^2 \rho(r), \quad (8)$$

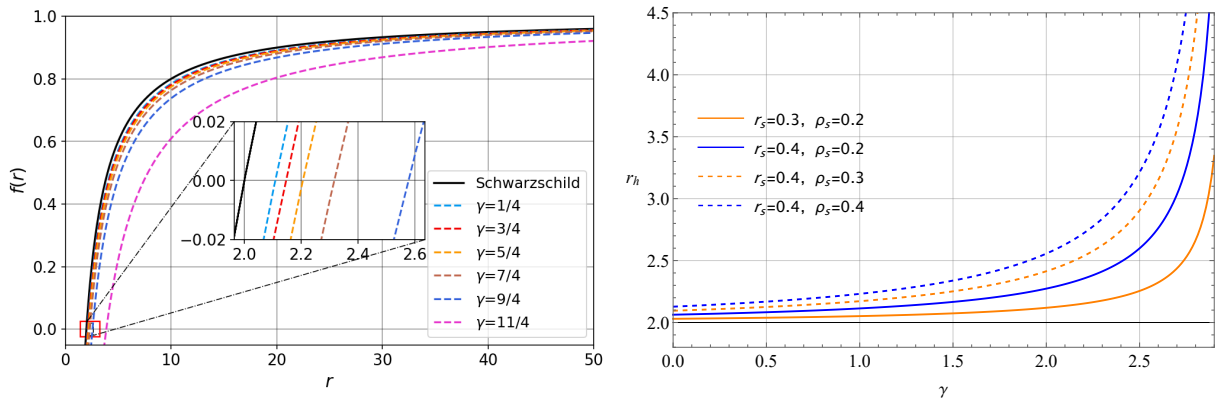


FIG. 1: Left panel: The radial dependence of function  $f(r)$  for various values of parameter  $\gamma$  for the fixed values of the DM halo parameters  $r_s = 0.4$  and  $\rho_s = 0.3$  values. Right panel: The dependence of horizon radius on  $\gamma$  for various combinations of  $r_s$  and  $\rho_s$ .

which solves to give

$$B(r) = 1 - \frac{8\pi}{r} \int r^2 \rho(r) dr = 1 - \frac{8\pi\rho_s r_s^3}{(3-\gamma)r} \left(\frac{r}{r+r_s}\right)^{3-\gamma} + \frac{C}{r}, \quad (9)$$

where  $C$  is an integration constant, taken as  $-2M$  provided that Eq.(9) reduces to the Schwarzschild case when the DM halo is absence. By imposing the condition  $P_r(r) = -\rho(r)$ , which implies  $A(r) = B(r)$ , the general spacetime metric, obtained as an exact solution of the field equations (4), can then be written as

$$ds^2 = -f(r)dt^2 + \frac{1}{f(r)}dr^2 + r^2(d\theta^2 + \sin^2\theta d\phi^2), \quad (10)$$

where

$$f(r) = 1 - \frac{2M}{r} - \frac{8\pi\rho_s r_s^3}{(3-\gamma)r} \left(\frac{r}{r+r_s}\right)^{3-\gamma}. \quad (11)$$

Using Eq. (11), we represent a number of the radial functions describing exact BH-DM solutions for specific various of the parameter  $\gamma$ , as tabulated in Table I.

We now turn to studying the behavior of  $f(r)$  and demonstrate its radial dependence in Fig. 1, highlighting how it changes depending on the parameter,  $\gamma$ , of Dehnen-type DM halo density profile. As can be seen from Fig. 1, the behavior of  $f(r)$  reduces to the flat spacetime at larger distances, especially at infinity. Furthermore, a systematic and progressively amplified movement of the curves towards larger  $r$ -values is observed with the growth of the parameter  $\gamma$ , resulting in an increase in the strength of the gravitational potential. The spacetime Eq. (11) has an event horizon, where a corotating observer's 4-velocity becomes null, resulting from setting  $f(r) = 0$ . As illustrated in the right panel of Fig. (1), the event horizon radius grows rapidly as the parameter  $\gamma$  and the DM halo parameters  $\rho_s$  and  $r_s$  increase.

$(\alpha, \beta, \gamma)$	$f(r)$
$(1, 4, 1/4)$	$1 - \frac{2M}{r} - \frac{32\pi\rho_s r_s^3}{11r} \left(\frac{r}{r+r_s}\right)^{11/4}$
$(1, 4, 3/4)$	$1 - \frac{2M}{r} - \frac{32\pi\rho_s r_s^3}{9r} \left(\frac{r}{r+r_s}\right)^{9/4}$
$(1, 4, 5/4)$	$1 - \frac{2M}{r} - \frac{32\pi\rho_s r_s^3}{7r} \left(\frac{r}{r+r_s}\right)^{7/4}$
$(1, 4, 7/4)$	$1 - \frac{2M}{r} - \frac{32\pi\rho_s r_s^3}{5r} \left(\frac{r}{r+r_s}\right)^{5/4}$
$(1, 4, 9/4)$	$1 - \frac{2M}{r} - \frac{32\pi\rho_s r_s^3}{3r} \left(\frac{r}{r+r_s}\right)^{3/4}$
$(1, 4, 11/4)$	$1 - \frac{2M}{r} - \frac{32\pi\rho_s r_s^3}{r} \left(\frac{r}{r+r_s}\right)^{1/4}$

TABLE I: Exact analytical Schwarzschild-like BH solutions describing static BHs surrounded by a DM halo with a Dehnen-type density profile  $(1, 4, \gamma)$ .

### III. THE SPACETIME CURVATURE AND ENERGY CONDITION CHARACTERISTICS

We now investigate the spacetime curvature invariants associated with a modified Schwarzschild-like BH immersed in a DM halo described by a Dehnen-type density profile. To perform this analysis, we compute the principal curvature invariants of the spacetime, namely the Ricci scalar  $R$ , the Ricci square  $R_{\mu\nu}R^{\mu\nu}$ , and the Kretschmann scalar  $R_{\mu\nu\alpha\beta}R^{\mu\nu\alpha\beta}$ . These invariants are analyzed in detail in order to determine the existence of a spacetime singularity at  $r = 0$ . We begin by examining the Ricci scalar for the combined BH-DM configuration, which, in this case, takes the form

$$R = \frac{8\pi(4-\gamma)r_s^5 \left(\frac{r_s+r}{r}\right)^\gamma \rho_s}{(r_s+r)^5}. \quad (12)$$

When the DM halo is absence (i.e.,  $\rho_s = 0$ ), the spacetime reduces to the Schwarzschild metric, where the Ricci is flat, i.e.  $R = 0$ . As for the Ricci square  $R^2$  and the Kretschmann scalar, they, respectively, take the forms

$$R^2 = \frac{32\pi^2 r_s^8 \rho_s^2 [(\gamma^2 - 4\gamma + 8)r_s^2 + 4\gamma r_s r + 8r^2]}{\left(\frac{r}{r_s+r}\right)^{2\gamma} (r_s+r)^{10}}, \quad (13)$$

and

$$K = \frac{48M^2}{r^6} - \frac{64\pi M r_s^3}{(\gamma-3)r^8} \left(\frac{r_s+r}{r}\right)^{\gamma-5} \times [6r^2 + 6(\gamma-1)rr_s + (\gamma-1)\gamma r_s^2] \rho_s + \mathcal{O}(\rho_s^2), \quad (14)$$

which reduces to the Schwarzschild case, i.e.,  $K = \frac{48M^2}{r^6}$ , in the absence of DM halo. From these expressions, we infer that the spacetime singularity is present at  $r = 0$ . The radial behavior of the curvature invariants is illustrated in Fig. 2, where singular nature of the spacetime clearly evident. Specifically, the curvature invariants vanish asymptotically as  $r \rightarrow \infty$ , while they diverge as  $r \rightarrow 0$

$$\lim_{r \rightarrow \infty} R, R_{\mu\nu}R^{\mu\nu}, R_{\mu\nu\alpha\beta}R^{\mu\nu\alpha\beta} \rightarrow 0, \quad (15)$$

and

$$\lim_{r \rightarrow 0} R, R_{\mu\nu}R^{\mu\nu}, R_{\mu\nu\alpha\beta}R^{\mu\nu\alpha\beta} \rightarrow \infty. \quad (16)$$

Similarly to the curvature invariants, the energy conditions represent important fundamental properties of spacetime. Here, we examine the relevant energy conditions to gain further insight into the physical nature of the NH-DM system. Subsequently, we proceed to solve Einstein's equations Eq. (4) in conjunction with the corresponding energy-momentum tensor  $T_\mu^\nu = \text{diag}[-\rho(r), P_r(r), P_\theta(r), P_\phi(r)]$ . Consequently, we derive the corresponding stress-energy tensor elements as

$$\rho(r) = -P_r(r) = \left(\frac{r_s}{r}\right)^4 \left(\frac{r+r_s}{r}\right)^{\gamma-4} \rho_s, \quad (17)$$

$$P_\theta(r) = P_\phi(r) = \frac{r_s^4 ((\gamma-2)r_s + 2r) \rho_s}{2(r_s+r)^5 \left(\frac{r}{r_s+r}\right)^\gamma}.$$

Based on the above equations, we further analyze the energy conditions associated with the DM halo source fluid. It is well known that the stress-energy tensor must satisfy a set of standard certain inequality constraints. Accordingly, we examine the null, weak, dominant, and strong energy conditions in this context:

- The null energy condition (NEC) is a fundamental requirement in general relativity, constraining the energy-momentum tensor such that the energy density along null directions remains non-negative, thereby excluding exotic phenomena associated with negative energy densities. Hence, the NEC leads to the condition [29, 46]:

$$T_{\mu\nu}n^\mu n^\nu \geq 0, \quad (18)$$

or

$$\rho(r) + P_i(r) \geq 0, \quad (i = r, \theta, \phi),$$

where  $n^\alpha$  refers to the null vector. From Eq. (17),  $P_r(r) + \rho(r) = 0$  reads

$$\rho(r) + P_\beta(r) = \frac{r_s^4 (\gamma r_s + 4r) \rho_s}{2(r_s+r)^5 \left(\frac{r}{r_s+r}\right)^\gamma} \geq 0, \quad (19)$$

where  $\beta = \theta, \phi$ . As can be seen from Eq. (19), it is obvious that it diverges as  $r \rightarrow 0$ , while it vanishes asymptotically as  $r \rightarrow \infty$

$$\lim_{r \rightarrow 0} [\rho(r) + P_\beta(r)] = \infty,$$

$$\lim_{r \rightarrow \infty} [\rho(r) + P_\beta(r)] = 0. \quad (20)$$

The behavior of the NEC is demonstrated in Fig 3 for various specific values of parameter  $\gamma$  while keeping DM halo parameters  $r_s$  and  $\rho_s$  fixed.

- Similarly, the weak energy condition (WEC) is a fundamental constraint in general relativity, requiring that the energy density measured by any time-like observer remains non-negative, i.e.,

$$\rho \geq 0, \quad \rho(r) + P_i(r) \geq 0, \quad (i = r, \theta, \phi). \quad (21)$$

We shown the behavior of the WEC in Fig. 3 for various values of  $\gamma$  for the fixed  $r_s$  and  $\rho_s$ .

- Next, we consider the dominant energy condition (DEC). This condition requires that for any future-directed causal vector field  $\mathbf{Y}^\nu$ , the vector  $-T_\nu^\mu \mathbf{Y}^\nu$  is likewise future-directed causal vector. As a stronger condition than the WEC, the DEC physically implies that the local energy density is non-negative and that energy flux propagation is restricted to subluminal speeds for all local observer. Specifically, the DEC is satisfied provided that

$$\rho(r) - |P_{\theta,\phi}| \geq 0,$$

Together with Eq. (17), this condition can be defined by

$$\frac{r_s^4 \rho_s \left(\frac{r_s+r}{r}\right)^\gamma}{r_s+r} \left( r+r_s - \left| r + \frac{1}{2}(\gamma-2)r_s \right| \right) \geq 0. \quad (22)$$

Similar behavior compared to previous energy conditions is also expected for various values of  $\gamma$  for the fixed  $r_s$  and  $\rho_s$ , as shown in Fig. 3.

- Finally, we consider the strong energy condition (SEC), which is determined by

$$\left( T_{\mu\nu} - \frac{1}{2} T g_{\mu\nu} \right) n^\mu n^\nu \geq 0 \quad \text{or} \quad \rho + \sum_{i=1}^3 P_i \geq 0, \quad (23)$$

which gives

$$\frac{r_s^4 ((\gamma-2)r_s + 2r) \rho_s}{(r_s+r)^5 \left(\frac{r}{r_s+r}\right)^\gamma} \geq 0. \quad (24)$$

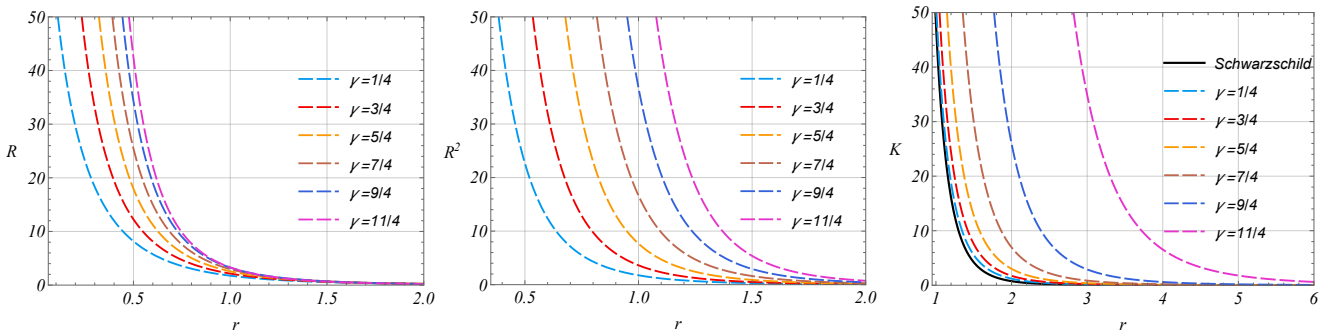


FIG. 2: The Ricci scalar ( $R$ ) (left panel), the Ricci square ( $R^2$ ) (middle panel), and the Kretschmann scalar ( $K$ ) (right panel) as a function of  $r$  for a Schwarzschild-like BH in a DM halo for different values of  $\gamma$  parameter

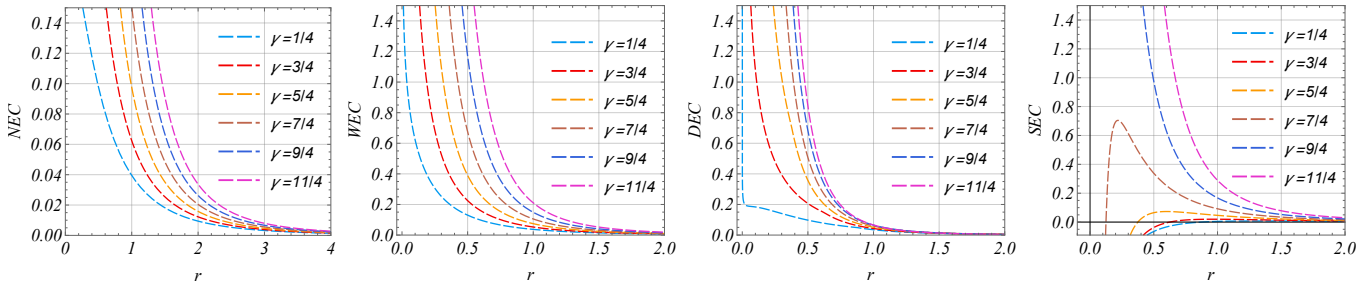


FIG. 3: The radial profile of the NEC, WEC, DEC and SEC for varying  $\gamma$  parameter (from left to right).

We present a detailed analysis of the radial behavior of the null, weak, dominant, and strong energy conditions (i.e., NEC, WEC, DEC, and SEC), as illustrated in Fig. 3. Results indicate that NEC, WEC and DEC are well satisfied for all specific values of the parameter  $\gamma$ , whereas the SEC is not fulfilled for cases, where  $\gamma < 2$ . This violation of the SEC for  $\gamma < 2$  is consistent with Eq. (24). Yet, the SEC would be satisfied for the specific values of DM halo parameters  $r_s$  and  $\rho_s$ . Here, our results suggest that all energy conditions are consistently satisfied for  $\gamma \geq 2$ .

#### IV. TIMELIKE AND NULL GEODESICS

To explore the impact of a DM halo on spacetime, we analyze the motion of massive particles and photons around a Schwarzschild-like BH embedded in a DM halo. Furthermore, we constrain the halo parameters  $r_s$  and  $\rho_s$  using observational data from the perihelion shifts of Mercury and the S2 star, together with the shadow measurements of M87\* and Sgr A\*. The dynamics of a particle in the spacetime of a Schwarzschild-like BH described by the metric (10) can be formulated within the Hamiltonian formalism [47]. The Hamiltonian is given by

$$H = \frac{1}{2} g^{\mu\nu} p_\mu p_\nu, \quad (25)$$

where  $p^\mu = m u^\mu$  is the four-momentum and  $u^\mu = dx^\mu/d\tau$  represents the four-velocity of the particle. In

spherical coordinates, the indices  $\mu$  and  $\nu$  run over the coordinate components  $(t, r, \theta, \phi)$ . For massive particles  $H = -m^2/2$ , while for photons  $H = 0$ . The equations of motion are obtained from Hamilton's equations

$$\frac{dx^\mu}{d\lambda} = \frac{\partial H}{\partial p_\mu} \quad \text{and} \quad \frac{dp_\mu}{d\lambda} = -\frac{\partial H}{\partial x^\mu}, \quad (26)$$

where  $\lambda = \tau/m$  is the affine parameter and  $\tau$  represents the proper time of the massive particle.

The spacetime metric (10) is independent of the coordinates  $t$  and  $\phi$ , leading to the conservation of the particle's energy and angular momentum, given by  $p_t = -E$  and  $p_\phi = L$  [47].

##### A. Dynamics of massive particle

Using Eq. (25) and conservation laws, the Hamiltonian for a massive particle can be written as

$$H = \frac{1}{2} (g^{rr} p_r^2 + g^{\theta\theta} p_\theta^2 + g^{tt} E^2 + g^{\phi\phi} L^2) = -\frac{m^2}{2}. \quad (27)$$

For simplicity, we assume that the massive particle moves in the equatorial plane  $\theta = \pi/2$ . From Eq. (10),  $g_{tt} = -f(r)$ ,  $g_{rr} = 1/f(r)$ , and  $g_{\phi\phi} = r^2$ . Substituting into Eq. (27), we obtain the equations governing the radial and azimuthal motion:

$$\left(\frac{dr}{d\tau}\right)^2 = \mathcal{E}^2 - f(r) \left(1 + \frac{\mathcal{L}^2}{r^2}\right) \quad \text{and} \quad \frac{d\phi}{d\tau} = \frac{\mathcal{L}}{r^2}, \quad (28)$$

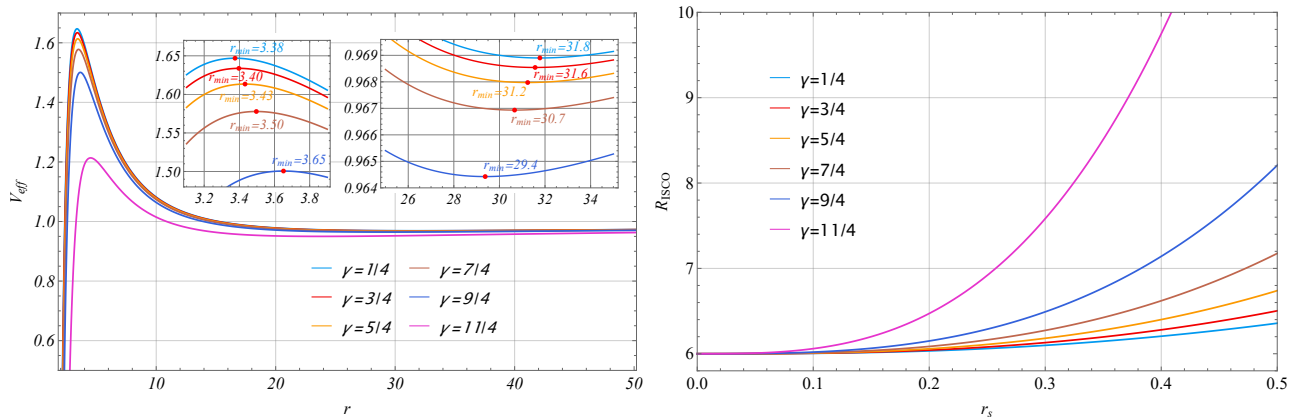


FIG. 4: The effective potential  $V_{\text{eff}}$  for the fixed  $r_s$  and  $\rho_s$  (left) and  $R_{\text{ISCO}}$  as a function of  $r_s$  for the fixed  $\rho_s$  (right) for various combinations of  $\gamma$ .

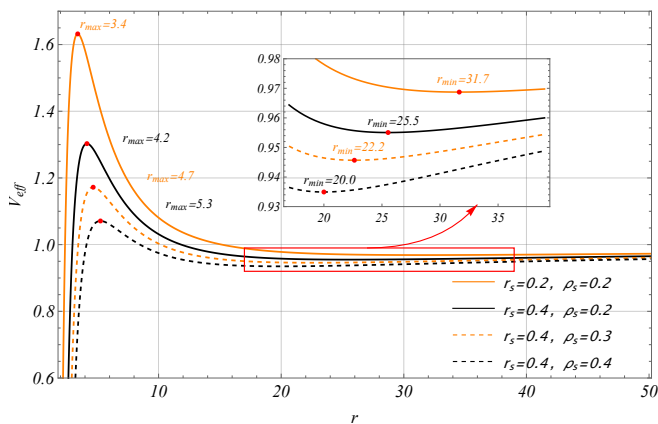


FIG. 5: Effective potential  $V_{\text{eff}}(r)$  for a massive particle for various combinations of  $r_s$  and  $\rho_s$ . Note that  $(\alpha, \beta, \gamma) = (1, 4, 9/4)$  is considered for the density profile.

where  $\mathcal{E} = E/m$  and  $\mathcal{L} = L/m$  represent the specific energy and specific angular momentum, respectively. From Eq. (28), the effective potential takes the general form

$$V_{\text{eff}}(r) = \left[ 1 - \frac{2M}{r} - \frac{8\pi\rho_s r_s^3}{(3-\gamma)r} \left( \frac{r}{r+r_s} \right)^{3-\gamma} \right] \times \left( 1 + \frac{\mathcal{L}^2}{r^2} \right). \quad (29)$$

Here, we choose the following density profile  $(\alpha, \beta, \gamma) = (1, 4, 9/4)$ , for which the effective potential becomes

$$V_{\text{eff}}^{(1,4,9/4)}(r) = \left[ 1 - \frac{2M}{r} - \frac{32\pi\rho_s r_s^3}{3r} \left( \frac{r}{r+r_s} \right)^{3/4} \right] \times \left( 1 + \frac{\mathcal{L}^2}{r^2} \right). \quad (30)$$

Using the above effective potential, the ISCO radius can be obtained from the conditions  $\frac{dV_{\text{eff}}}{dr} = 0$  and  $\frac{d^2V_{\text{eff}}}{dr^2} = 0$  [48, 49].

Fig. 4 shows the effective potential and  $R_{\text{ISCO}}$  for the density profile  $(\alpha, \beta, \gamma) = (1, 4, \gamma)$ . As seen from the figure, with increasing  $\gamma$ , the height of the effective potential decreases, and the location of the unstable orbit (corresponding to the maximum of the effective potential) shifts toward larger values of  $r$ . In addition,  $R_{\text{ISCO}}$  increases with increasing  $\gamma$  for a given value of  $r_s$ . This suggests that the gravitational effects become stronger as  $\gamma$  increases. Fig. 5 shows the effective potential for the density profile  $(1, 4, 9/4)$  for different values of DM halo parameters, i.e.,  $r_s$  and  $\rho_s$ . We observe that with increasing  $r_s$  and  $\rho_s$ , the unstable orbits shift outward, while the stable orbits (minima of the effective potential) shift inward.

By combining Eqs. (28) and (30), the trajectory equation can be expressed as

$$\left( \frac{dr}{d\phi} \right)^2 = \frac{r^4 \left( \mathcal{E}^2 - V_{\text{eff}}^{(1,4,9/4)}(r) \right)}{\mathcal{L}^2}. \quad (31)$$

Introducing the transformation  $u = 1/r$  and differentiating with respect to  $\phi$ , the trajectory equation becomes

$$\frac{d^2u}{d\phi^2} = \frac{M}{\mathcal{L}^2} - u + \frac{g(u)}{\mathcal{L}^2}, \quad (32)$$

where

$$\frac{g(u)}{\mathcal{L}^2} = 3Mu^2 + 4\pi\rho_s r_s^3 \left( \frac{1}{1+r_s u} \right)^{7/4} \times \frac{(4 + u(r_s + 12uL^2 + 9r_s u^2 L^2))}{3L^2}. \quad (33)$$

Adopting the procedure outlined in Ref. [50], the perihelion shift after one orbital period is given by

$$\Delta\phi = \frac{\pi}{\mathcal{L}^2} \left| \frac{dg(u)}{du} \right|_{u=\frac{1}{b}}, \quad (34)$$

where  $b = a(1 - e^2)$ , in which  $a$  and  $e$  correspond to the semi-major axis and the eccentricity of the orbit. In

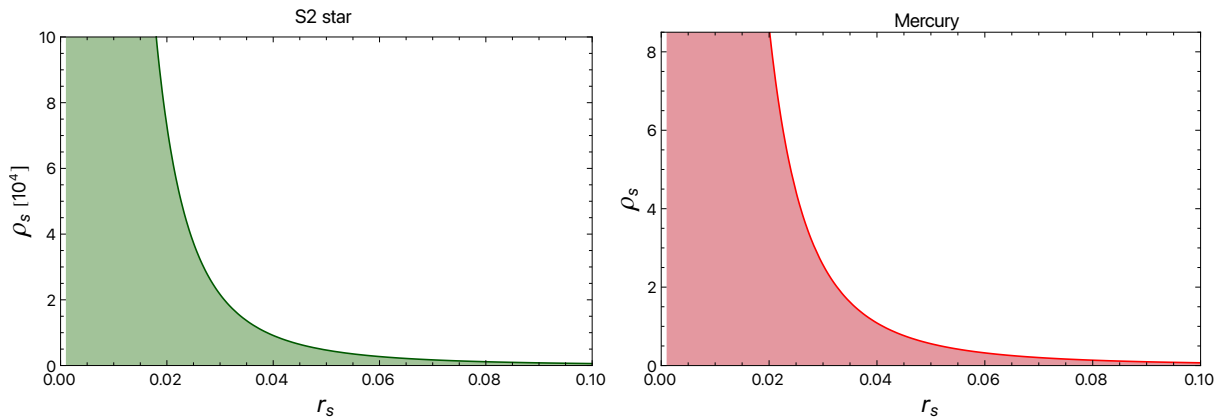


FIG. 6: Parameter space of the dimensionless halo radius  $r_s$  and characteristic density  $\rho_s$ . The shaded regions represent the observationally allowed values of  $(r_s, \rho_s)$  inferred from S2 star (left panel) and Mercury (right panel) measurements.

order to recover the physical dimensions, the quantities  $M$ ,  $L^2$ , the DM halo characteristic density  $\rho_s$ , and the scale radius  $r_s$  are rescaled according to

$$M \Rightarrow GM/c^2, \quad (35)$$

$$L^2 \Rightarrow GMa(1 - e^2)/c^2, \quad (36)$$

$$\rho_s \Rightarrow \frac{3c^4}{32\pi G^2 M^2} \rho_s, \quad (37)$$

$$r_s \Rightarrow \frac{GM}{c^2} r_s. \quad (38)$$

where  $\rho_s$  and  $r_s$  on the right-hand side are dimensionless. Using the above equations together with Eq. (34), the perihelion shift after one complete revolution can be written as

$$\Delta\phi = 6\pi\alpha + \frac{3\pi\alpha}{32} \rho_s r_s^3 \left( \frac{1}{1 + \alpha r_s} \right)^{11/4} \times (32 - 8(1 - 5\alpha)r_s - \alpha(1 - 15\alpha)r_s^2), \quad (39)$$

where

$$\alpha = \frac{GM}{ac^2(1 - e^2)}. \quad (40)$$

We proceed to analyze an astronomical application of the perihelion shift. In particular, we use observational data from the perihelion shifts of Mercury and the S2 star to constrain the parameters  $\rho_s$  and  $r_s$ . The orbital parameters and observed perihelion shifts of Mercury and the S2 star adopted in this work are as follows

#### Mercury:

$$\frac{2GM_\odot}{c^2} = 2.95325008 \times 10^3 \text{ [m]},$$

$$a = 5.7909175 \times 10^{10} \text{ [m]},$$

$$e = 0.20563069,$$

$$\Delta\phi_{\text{obs}} = 2\pi \times (7.98734 \pm 0.00037) \times 10^{-8} \text{ rad/rev.}$$

#### S2 star:

$$M_{\text{Sgr A}^*} = 4.260 \times 10^6 M_\odot,$$

$$a_{\text{S2}} = 970 \text{ [au]},$$

$$1 \text{ au} = 1.495978707 \times 10^{11} \text{ [m]},$$

$$e_{\text{S2}} = 0.884649,$$

$$T_{\text{S2}} = 16.052 \text{ [years]},$$

$$\Delta\phi_{\text{obs}} = 48.298 f_{\text{SP}} \left[ \text{''/year} \right], \quad f_{\text{SP}} = 1.10 \pm 0.19.$$

Using these data and Eq. (39), we plot the parameter space of  $\rho_s$  and  $r_s$  for Mercury and the S2 star (Fig. 6). It can be seen from Fig. 6 that the allowed region associated with the S2 star is larger than that obtained for Mercury. This shows that the effect of the DM halo is more pronounced around more massive objects. In particular, the characteristic scale of  $\rho_s$  for Mercury is about  $10^4$  times smaller than that for the S2 star. This suggests that DM halo effects may be observable primarily around supermassive BHs.

## B. Photon geodesics

We now investigate the null geodesics around the Schwarzschild-like BH surrounded by DM halo characterized by  $(\alpha, \beta, \gamma) = (1, 4, 9/4)$ . The four-momentum of a photon can be written as

$$p^\alpha = dx^\alpha/d\lambda. \quad (41)$$

As in the massive particle case, we restrict the motion to the plane  $\theta = \pi/2$ . Using Eqs. (25), (26) together with the conservation laws, we obtain the following equation governing the propagation of light.

$$\frac{dt}{d\lambda} = \frac{E}{f(r)} \quad \text{and} \quad \frac{d\phi}{d\lambda} = \frac{L}{r^2}, \quad (42)$$

$$\left( \frac{dr}{d\lambda} \right)^2 = E^2 - f(r) \frac{L^2}{r^2}. \quad (43)$$

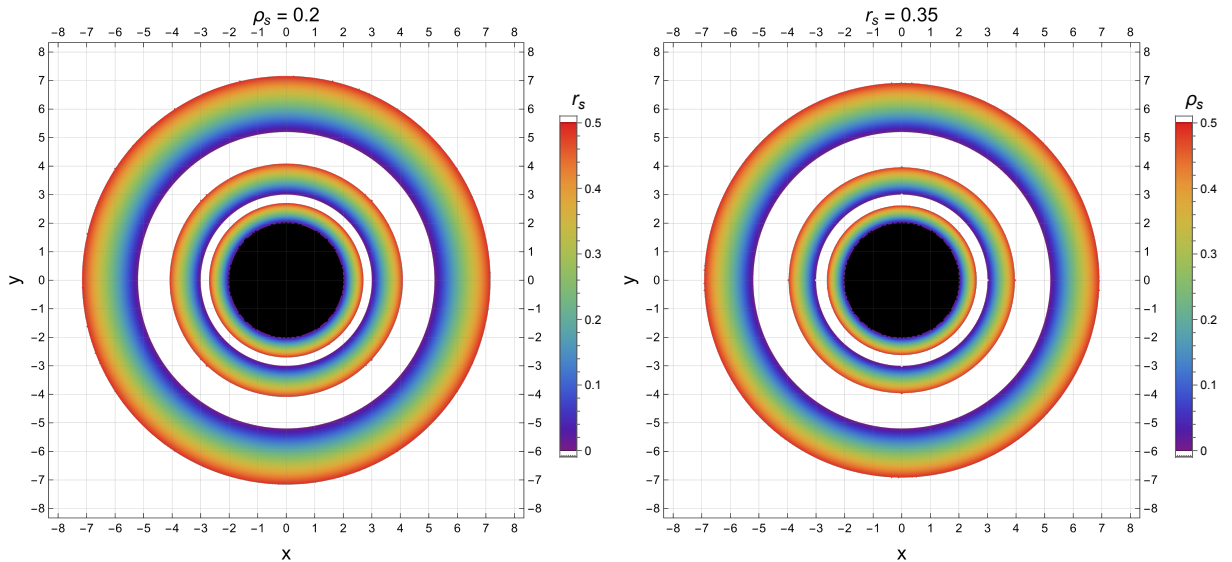


FIG. 7: Shadow structure of Schwarzschild BH in the presence of a DM halo. The central black disk represents the event horizon of the Schwarzschild BH. The innermost colored ring illustrates how the horizon radius varies with the DM halo parameters, while the middle ring corresponds to the photon sphere. The outermost ring represents the BH shadow. The color scale indicates the values of the DM halo parameters: the scale radius  $r_s$  (left panel) and the characteristic density  $\rho_s$  (right panel).

Introducing the transformation  $\lambda' = L\lambda$ , the above equations can be rewritten as

$$\frac{dt}{d\lambda'} = \frac{1}{bf(r)} \quad \text{and} \quad \frac{d\phi}{d\lambda'} = \frac{1}{r^2}, \quad (44)$$

$$\left(\frac{dr}{d\lambda'}\right)^2 = \frac{1}{b^2} - \frac{f(r)}{r^2} = V_{\text{eff}}^{\text{ph}}(r), \quad (45)$$

where  $b = L/E$  denotes the impact parameter, and  $V_{\text{eff}}^{\text{ph}}$  represents the effective potential for photons. The radius  $r_{\text{ph}}$  of the photon sphere is defined by

$$\frac{d}{dr} \left( V_{\text{eff}}^{\text{ph}}(r) \right) = 0 \quad (46)$$

Since the solution of the above equation is complicated, we solve it numerically and present the radii of the photon sphere for different values of  $\rho_s$  and  $r_s$  in Table II.

$\rho_s \backslash r_s$	0.0	0.1	0.2	0.3	0.4	0.5
0.0	3.0000	3.00000	3.00000	3.00000	3.00000	3.00000
0.1	3.0000	3.00487	3.03774	3.12392	3.28715	3.55166
0.2	3.0000	3.00973	3.07554	3.24867	3.57932	4.12205
0.3	3.0000	3.01460	3.11340	3.37416	3.87559	4.70550
0.4	3.0000	3.01946	3.15130	3.50033	4.17520	5.29827
0.5	3.0000	3.02433	3.18926	3.62711	4.47759	5.89785

TABLE II: Photon sphere radius  $r_{\text{ph}}$  for different values of  $\rho_s$  and  $r_s$ .

For a distant observer, the radius of the BH shadow is determined by the critical impact parameter of photon trajectories,  $R_{\text{sh}} = b_c$ . A photon coming from infinity with  $b = b_c$  asymptotically approaches the photon

sphere, and therefore the apparent radius of the shadow corresponds to this critical impact parameter. This critical impact parameter  $b_c$  is obtained from the condition  $V_{\text{eff}}^{\text{ph}}(r_{\text{ph}}) = 0$  and is given by

$$R_{\text{sh}} = b_c = \frac{r_{\text{ph}}}{\sqrt{f(r_{\text{ph}})}}. \quad (47)$$

Fig. 7 illustrates the shadow, photon sphere, and horizon structure of the Schwarzschild-like BH in the presence of DM halo. Table II lists the corresponding numerical values of  $r_{\text{ph}}$ . It is observed that the radii of the shadow, photon sphere, and horizon increase with increasing  $r_s$  and  $\rho_s$ . This behavior indicates that the DM halo enhances the effective gravitational field around the BH.

## V. PARAMETER ESTIMATION FOR BH PARAMETERS IN DM HALO

The observable quantity measured in astronomical observations is the angular diameter of the BH shadow,  $\theta_{\text{sh}}$ , which is related to the dimensionless shadow radius  $R_{\text{sh}}$  by

$$\theta_{\text{sh}} = R_{\text{sh}} \times \frac{2GM}{c^2 D}, \quad (48)$$

where  $D$  denotes the distance between the observer and the BH.

Using observational data for Sgr A\* and M87\* listed in Table III, we constrain the mass  $M$ , the characteristic density  $\rho_s$ , and the scale radius  $r_s$  of the DM halo through

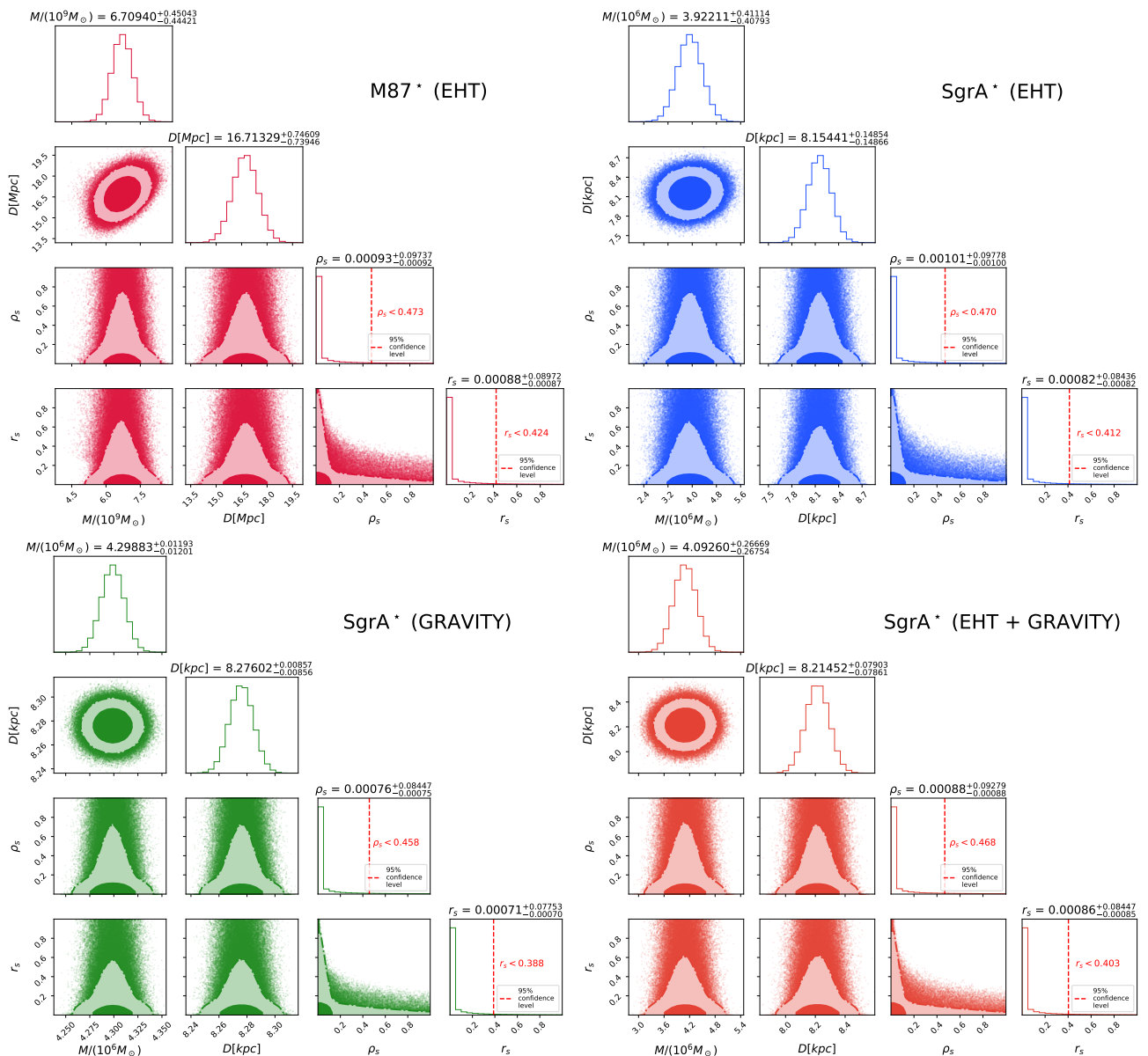


FIG. 8: Posterior probability distributions for the BH mass ( $M$ ), distance ( $D$ ), DM halo density ( $\rho_s$ ), and halo scale radius ( $r_s$ ), obtained from the shadow observations of Sgr A\* and M87\*. The vertical red dashed lines indicate the 95% confidence levels on  $\rho_s$  and  $r_s$ .

Object	$\theta_{sh}$ ( $\mu\text{as}$ )	Distance $D$	Mass $M$	Data
M87*	$42 \pm 3$	$16.8 \pm 0.8$ Mpc	$(6.5 \pm 0.7) \times 10^9 M_\odot$	EHT
Sgr A*	$48.7 \pm 7$	$8150 \pm 150$ pc	$(4.0^{+1.1}_{-0.6}) \times 10^6 M_\odot$	EHT
Sgr A*	—	$8275.9 \pm 8.6$ pc	$(4.299 \pm 0.012) \times 10^6 M_\odot$	GRAVITY

TABLE III: Observed parameters for the supermassive BHs M87\* and Sgr A\* (see details in [51–53]).

an MCMC analysis. The parameter space is explored using the Python package *emcee* [54], which implements Markov Chain Monte Carlo (MCMC) sampling.

The likelihood function quantifies how well the theo-

retical prediction of the angular shadow  $\theta_{sh}^{theory}$  agrees with the observational measurement  $\theta_{sh}^{obs}$  for a given set of model parameters. The logarithmic likelihood function is therefore written as

$$\log \mathcal{L}(M, D, \rho_s, r_s) = -\frac{1}{2} \left( \frac{\theta_{sh}^{theory}(M, \rho_s, r_s) - \theta_{sh}^{obs}}{\sigma_{sh}^{obs}} \right)^2, \quad (49)$$

where  $\sigma_{sh}^{obs}$  represents the corresponding observational uncertainty.

For the parameters  $M$  and  $D$ , we assume Gaussian priors centered at their measured values with standard deviations corresponding to their respective observational

Parameter	M87 (EHT)	Sgr A* (EHT)	Sgr A* (GRAVITY)	Sgr A* (EHT+GRAVITY)
$M$	$6.70940^{+0.45043}_{-0.44421} \times 10^9 M_\odot$	$3.92211^{+0.41114}_{-0.40793} \times 10^6 M_\odot$	$4.29883^{+0.01193}_{-0.01201} \times 10^6 M_\odot$	$4.09260^{+0.26669}_{-0.26754} \times 10^6 M_\odot$
$D$	$16.71329^{+0.74609}_{-0.73946} \text{ Mpc}$	$8.15441^{+0.14854}_{-0.14866} \text{ kpc}$	$8.27602^{+0.00857}_{-0.00856} \text{ kpc}$	$8.21452^{+0.07903}_{-0.07861} \text{ kpc}$
$\rho_s$	$0.00093^{+0.09737}_{-0.00092}$	$0.00101^{+0.09778}_{-0.00100}$	$0.00076^{+0.08447}_{-0.00075}$	$0.00088^{+0.09279}_{-0.00088}$
$r_s$	$0.00088^{+0.08972}_{-0.00087}$	$0.00082^{+0.08436}_{-0.00082}$	$0.00071^{+0.07753}_{-0.00070}$	$0.00086^{+0.08447}_{-0.00085}$
$\rho_s$ (95% C.L.)	$\rho_s < 0.473$	$\rho_s < 0.470$	$\rho_s < 0.458$	$\rho_s < 0.468$
$r_s$ (95% C.L.)	$r_s < 0.424$	$r_s < 0.412$	$r_s < 0.388$	$r_s < 0.403$

TABLE IV: Best-fit values and upper limits of the model parameters obtained from the MCMC analysis for M87\* and Sgr A\*. The quoted uncertainties correspond to the 68% confidence intervals, while the upper limits for  $\rho_s$  and  $r_s$  are given at the 95% confidence level.

uncertainties. The prior distribution can therefore be written as

$$\pi(\theta_i) \propto \exp \left[ -\frac{1}{2} \left( \frac{\theta_i - \theta_{0,i}}{\sigma_i} \right)^2 \right], \quad (50)$$

where  $\theta_i = [M, D]$ ,  $\theta_{0,i}$  denotes the measured value of the parameter, and  $\sigma_i$  is the corresponding observational uncertainty. For the remaining parameters  $\rho_s$  and  $r_s$ , we assume independent uniform priors in the interval  $[0, 1]$ ,

$$\pi(\rho_s, r_s) = \begin{cases} 1, & 0 \leq \rho_s \leq 1, 0 \leq r_s \leq 1, \\ 0, & \text{otherwise.} \end{cases} \quad (51)$$

The posterior probability distribution of the model parameters  $\Theta = (M, D, \rho_s, r_s)$  is obtained using Bayes' theorem, which combines the likelihood function with the prior distributions. It can be written as

$$P(\Theta|\mathcal{D}) = \frac{\mathcal{L}(\mathcal{D}|\Theta) \pi(\Theta)}{\mathcal{Z}}, \quad (52)$$

where  $\mathcal{D}$  denotes the observational data,  $\mathcal{L}$  is the likelihood function,  $\pi(\Theta)$  represents the joint prior distribution of the parameters, and  $\mathcal{Z}$  serves as a normalization constant.

Fig. 8 shows the posterior distributions for Sgr A\* and M87\*. The shaded contours correspond to the 68% and 95% confidence levels. The red vertical dashed lines indicate the 95% upper limits on the DM halo parameters  $\rho_s$  and  $r_s$ . The best-fit values and corresponding upper limits of the BH parameters are summarized in Table IV.

Fig. 9 illustrates the consistency between the model predictions and the observational data. In all cases, the best-fit model values lie within the observational uncertainties of  $M$ ,  $D$ , and  $\theta_{\text{sh}}$ . Our results suggest that the best-fit values inferred from the EHT dataset show good agreement with the observed values, whereas the GRAVITY and combined datasets provide tighter constraints on the DM halo parameters.

## VI. CONCLUSION

Given that DM constitutes the dominant mass component of galaxies, its interaction with BHs at galactic centers can significantly influence the spacetime geometry in their vicinity. In particular, the presence of a DM halo may modify key observables such as orbital dynamics, gravitational lensing, and BH shadows. Therefore, investigating BH–DM systems not only deepens our understanding of BH environments but also provides a means to probe and constrain the properties and distribution of DM halo. Based on these considerations, we derived a new set of analytical Schwarzschild-like BH solutions that describe a static BH surrounded by a DM halo with a Dehnen-type density profile  $(1, 4, \gamma)$ .

We investigated the properties of these BH–DM systems through their spacetime curvature, computing curvature invariants to characterize the singularity in the solution. Our analysis showed the presence of a spacetime singularity at  $r = 0$ , as shown in Fig. 2. We further assessed the physical viability of the spacetime by examining the energy conditions associated with the DM halo. The results showed that all energy conditions are well satisfied for the derived solutions with the chosen DM halo parameters, except for the strong energy condition (SEC), which remains satisfied only for  $\gamma \geq 2$ . This conclusion is supported by the results illustrated in Fig. 3

We further explored timelike and null geodesics in the BH–DM spacetime to examine how the derived analytical solutions influence the motion of massive and massless particles. From the analysis of the effective potential and the ISCO, we found that the ISCO radius  $R_{\text{ISCO}}$  increases with increasing density profile parameter  $\gamma$  and DM scale radius  $r_s$ , indicating stronger gravitational effects. Moreover, increasing the DM halo parameters  $r_s$  and  $\rho_s$  shifted the unstable orbits outward, while the stable orbits moved inward (see Figs. 4, 5). Using observational data from the trajectories of Mercury and the S2 star, we determined the allowed parameter space  $(r_s, \rho_s)$  for the chosen DM halo density profile  $(\alpha, \beta, \gamma) = (1, 4, 9/4)$  and showed that its effects are more pronounced around supermassive BHs than in the solar

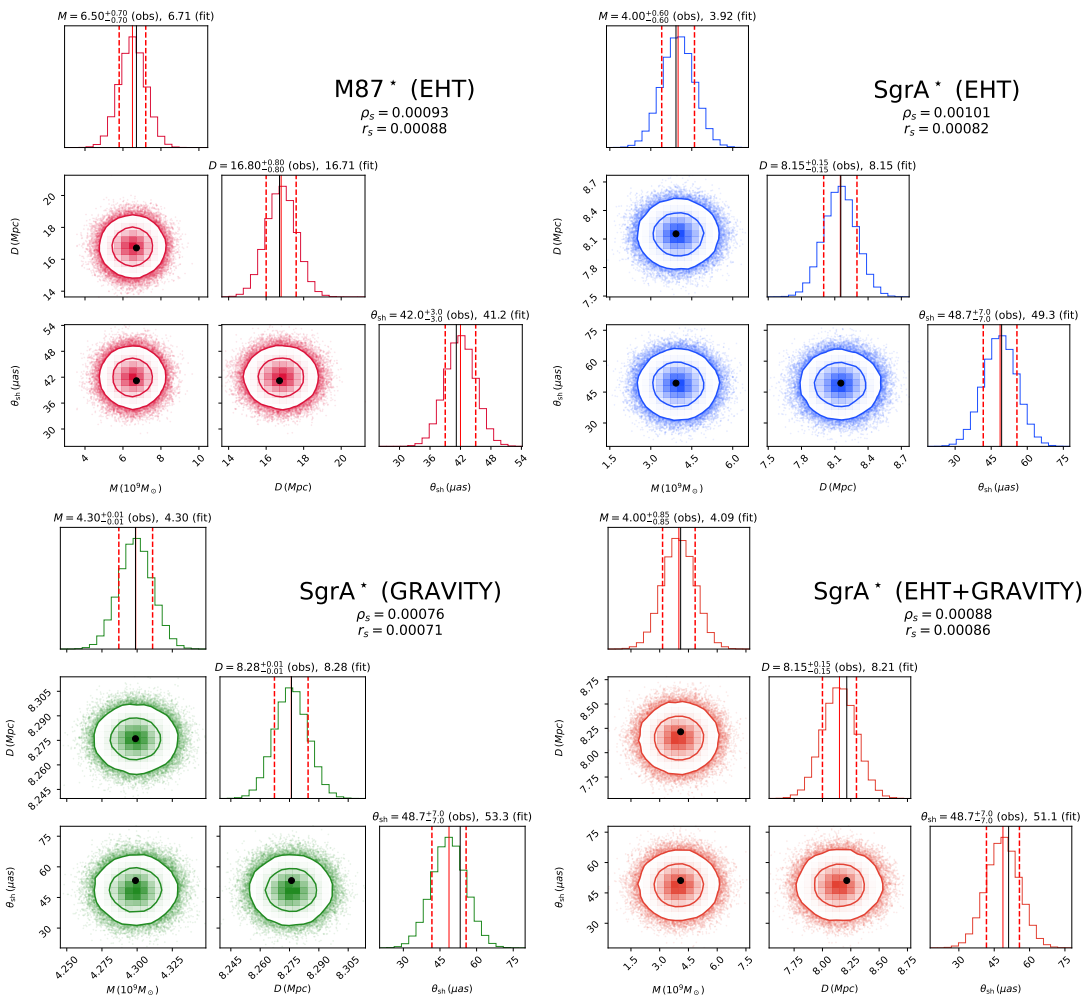


FIG. 9: Comparison between model predictions and observational data for the BH mass  $M$ , distance  $D$ , and shadow angular diameter  $\theta_{\text{sh}}$  for M87\* and Sgr A\* using EHT, GRAVITY, and combined (EHT+GRAVITY) datasets. The shaded regions represent the observational distributions. The solid vertical lines indicate the central observed values, while the dashed lines denote the corresponding uncertainties. The black vertical lines and dots mark the best-fit model predictions. The associated values of the DM halo parameters  $\rho_s$  and  $r_s$  are displayed in each panel.

system (see Fig. 6). The analysis of the shadow, photon sphere, and horizon structures showed that their radii increase with increasing  $r_s$  and  $\rho_s$ , reflecting the enhanced gravitational influence due to the DM halo (see Fig. 7 and Table II).

Finally, using observational data for Sgr A\* and M87\*, we constrained the characteristic density  $\rho_s$  and the halo scale radius  $r_s$  of the DM halo through an MCMC analysis. The resulting posterior distributions provided the best-fit values and upper limits for the model parameters. We found that the best-fit values were consistent with the observational uncertainties of  $M$ ,  $D$ , and  $\theta_{\text{sh}}$ . In particular, the results based on the EHT dataset exhibited good

agreement with the observed values, while the GRAVITY and combined (EHT+GRAVITY) datasets provided comparatively tighter constraints on the DM halo parameters (see Figs. 8, 9).

Overall, our results for the novel exact BH-DM halo solutions highlight the role of DM halos in modifying the spacetime geometry and observable properties of astrophysical BHs, offering a new perspective on BH-DM interactions. Our findings demonstrate that observations of BH shadows and particle dynamics can be used to probe and constrain the properties of DM halo in the vicinity of supermassive BHs.

[1] K. Akiyama and et al. (Event Horizon Telescope Collaboration), *Astrophys. J.* **875**, L1 (2019), 1906.11238.

[2] K. Akiyama and et al. (Event Horizon Telescope Collab-

- oration), *Astrophys. J. Lett.* **930**, L12 (2022).
- [3] B. P. Abbott and et al. (Virgo and LIGO Scientific Collaborations), *Phys. Rev. Lett.* **116**, 061102 (2016), 1602.03837.
  - [4] B. P. Abbott and et al. (Virgo and LIGO Scientific Collaborations), *Phys. Rev. Lett.* **116**, 241102 (2016), 1602.03840.
  - [5] F. Iocco, M. Pato, and G. Bertone, *Nature Phys.* **11**, 245 (2015), 1502.03821.
  - [6] G. Bertone and T. M. P. Tait, *Nature* **562**, 51 (2018), 1810.01668.
  - [7] V. C. Rubin and J. Ford, W. Kent, *Astrophys. J.* **159**, 379 (1970).
  - [8] E. Corbelli and P. Salucci, *Mon. Not. Roy. Astron. Soc.* **311**, 441 (2000), astro-ph/9909252.
  - [9] M. Davis, G. Efstathiou, C. S. Frenk, and S. D. M. White, *Astrophys. J.* **292**, 371 (1985).
  - [10] M. Persic, P. Salucci, and F. Stel, *Mon. Not. R. Astron. Soc.* **281**, 27 (1996), astro-ph/9506004.
  - [11] M. Valluri, D. Merritt, and E. Emsellem, *Astrophys. J.* **602**, 66 (2004), astro-ph/0210379.
  - [12] K. Akiyama and et al. (Event Horizon Telescope Collaboration), *Astrophys. J.* **875**, L6 (2019), 1906.11243.
  - [13] C. Boehm and P. Fayet, *Nucl. Phys. B* **683**, 219 (2004), hep-ph/0305261.
  - [14] G. Bertone, D. Hooper, and J. Silk, *Phys. Rep.* **405**, 279 (2005), hep-ph/0404175.
  - [15] J. L. Feng, M. Kaplinghat, H. Tu, and H.-B. Yu, *J. Cosmol. Astropart. Phys.* **2009**, 004 (2009), 0905.3039.
  - [16] M. Schumann, *J. Phys. G Nucl. Part. Phys.* **46**, 103003 (2019), 1903.03026.
  - [17] S. Babak, J. Gair, A. Sesana, E. Barausse, C. F. Sopuerta, C. P. L. Berry, E. Berti, P. Amaro-Seoane, A. Petiteau, and A. Klein, *Phys. Rev. D* **95**, 103012 (2017), 1703.09722.
  - [18] D. A. Brown, J. Brink, H. Fang, J. R. Gair, C. Li, G. Lovelace, I. Mandel, and K. S. Thorne, *Phys. Rev. Lett.* **99**, 201102 (2007), gr-qc/0612060.
  - [19] P. Amaro-Seoane, *Phys. Rev. D* **98**, 063018 (2018), 1807.03824.
  - [20] D. Clowe, M. Bradač, A. H. Gonzalez, M. Markevitch, S. W. Randall, C. Jones, and D. Zaritsky, *Astrophys. J. Lett.* **648**, L109 (2006), astro-ph/0608407.
  - [21] D. Merritt, A. W. Graham, B. Moore, J. Diemand, and B. Terzić, *Astron. J.* **132**, 2685 (2006), astro-ph/0509417.
  - [22] A. A. Dutton and A. V. Macciò, *Mon. Not. Roy. Astron. Soc.* **441**, 3359–3374 (2014), ISSN 0035-8711, URL <http://dx.doi.org/10.1093/mnras/stu742>.
  - [23] J. F. Navarro, C. S. Frenk, and S. D. M. White, *Astrophys. J.* **462**, 563 (1996), ISSN 1538-4357, URL <http://dx.doi.org/10.1086/177173>.
  - [24] A. Burkert, *Astrophys. J.* **447** (1995), ISSN 0004-637X, URL <http://dx.doi.org/10.1086/309560>.
  - [25] W. Dehnen, *Mon. Not. R. Astron. Soc.* **265**, 250 (1993).
  - [26] Shukirgaliyev, B., Otebay, A., Sobolenko, M., Ishchenko, M., Borodina, O., Panamarev, T., Myrzakul, S., Kalambay, M., Naurzbayeva, A., Abdikamalov, E., et al., *Astron. Astrophys.* **654**, A53 (2021), URL <https://doi.org/10.1051/0004-6361/202141299>.
  - [27] M. M. Gohain, P. Phukon, and K. Bhuyan, *Phys. Dark Univ.* **46**, 101683 (2024), 2407.02872.
  - [28] R. C. Pantig and A. Övgün, *J. Cosmol. Astropart. Phys.* **2022**, 056 (2022), 2202.07404.
  - [29] A. Al-Badawi, S. Shaymatov, and Y. Sekhmani, *J. Cosmol. Astropart. Phys.* **2025**, 014 (2025), 2411.01145.
  - [30] U. Uktamov, S. Shaymatov, B. Ahmedov, and C. Yuan, *Eur. Phys. J. C* **85**, 1432 (2025), 2505.20031.
  - [31] M.-H. Li and K.-C. Yang, *Phys. Rev. D* **86**, 123015 (2012), 1204.3178.
  - [32] S. Shaymatov, B. Ahmedov, and M. Jamil, *Eur. Phys. J. C* **81**, 588 (2021).
  - [33] S. Shaymatov, D. Malafarina, and B. Ahmedov, *Phys. Dark Universe* **34**, 100891 (2021), 2004.06811.
  - [34] S. Shaymatov, P. Sheoran, and S. Siwach, *Phys. Rev. D* **105**, 104059 (2022), 2110.10610.
  - [35] V. Cardoso, K. Destounis, F. Duque, R. P. Macedo, and A. Maselli, *Phys. Rev. D* **105**, L061501 (2022), 2109.00005.
  - [36] X. Hou, Z. Xu, M. Zhou, and J. Wang, *J. Cosmol. Astropart. Phys.* **2018**, 015 (2018), 1804.08110.
  - [37] Z. Shen, A. Wang, Y. Gong, and S. Yin, *Phys. Lett. B* **855**, 138797 (2024), 2311.12259.
  - [38] Z. Shen, A. Wang, and S. Yin, *Phys. Lett. B* **862**, 139300 (2025), 2408.05417.
  - [39] A. Al-Badawi and S. Shaymatov, *Chin. Phys. C* **49**, 055101 (2025), 2501.15397.
  - [40] A. Al-Badawi and S. Shaymatov, *Commun. Theor. Phys.* **77**, 035402 (2025).
  - [41] M. Alloqulov, T. Xamidov, S. Shaymatov, and B. Ahmedov, arXiv e-prints arXiv:2504.05236 (2025), 2504.05236.
  - [42] T. Xamidov, U. Uktamov, S. Shaymatov, and B. Ahmedov, *Phys. Dark Universe* **47**, 101805 (2025).
  - [43] T. Xamidov, S. Shaymatov, Q. Wu, and T. Zhu, *Eur. Phys. J. C* **85**, 1193 (2025), 2507.13147.
  - [44] H. Mo, F. C. van den Bosch, and S. White, *Galaxy Formation and Evolution* (Cambridge University Press, Cambridge, 2010).
  - [45] Z. Xu, X. Hou, X. Gong, and J. Wang, *J. Cosmol. Astropart. Phys.* **2018**, 038 (2018), 1803.00767.
  - [46] B. Toshmatov, C. Bambi, B. Ahmedov, A. Abdujabbarov, and Z. Stuchlík, *European Physical Journal C* **77**, 542 (2017), 1702.06855.
  - [47] C. W. Misner, K. S. Thorne, and J. A. Wheeler, *Gravitation* (W. H. Freeman, San Francisco, 1973).
  - [48] N. Dadhich and S. Shaymatov, *Phys. Dark Universe* **35**, 100986 (2022), 2104.00427.
  - [49] N. Dadhich and S. Shaymatov, *Int. J. Mod. Phys. D* **31**, 2150120 (2022).
  - [50] G. S. Adkins and J. McDonnell, *Phys. Rev. D* **75**, 082001 (2007), gr-qc/0702015.
  - [51] Event Horizon Telescope Collaboration and Akiyama, *Astrophys. J.* **875**, L6 (2019), 1906.11243.
  - [52] Event Horizon Telescope Collaboration and K. Akiyama, *Astrophys. J. Lett.* **930**, L12 (2022).
  - [53] Gravity Collaboration and K. Abd El Dayem, *Astron. Astrophys.* **692**, A242 (2024), 2409.12261.
  - [54] D. Foreman-Mackey, D. W. Hogg, D. Lang, and J. Goodman, *Publ. Astron. Soc. Pac.* **125**, 306 (2013), 1202.3665.